Advanced Processing of Measured Fields using Field Reconstruction Techniques

Erik Jørgensen, Peter Meincke, Cecilia Cappellin
TICRA
Læderstræde 34, DK-1201, Denmark
ej@ticra.com, pme@ticra.com, cc@ticra.com

***Abstract*—This contribution deals with the problem of reconstructing the extreme near-field of an antenna starting from the field measured at a larger distance. The presented method has several applications, including but not limited to antenna diagnostics, suppression of spurious contributions from the measurement system, or artificial removal the currents flowing on mounting structures or cables. The capabilities are illustrated by processing of field data obtained from spherical near-field measurements of a horn antenna and a radiometer antenna mounted on a satellite.**

I. Introduction

In the last decade there has been a growing research effort aimed at reconstructing the extreme near field of an antenna from the field measured in a classical near-field measurement acquisition system. Several new methods have emerged, including mode-based methods such as the SWE-PWE method [1], or methods based on discretization of integral equations [2]- [15], e.g., the source reconstruction method (SRM) and the Inverse Method of Moments (INV-MoM). A common property of these new methods is that there is no theoretical limit on the resolution whereas the resolution in practical environments is limited by the noise level of the measured data. The classical application area of these methods is antenna diagnostics where electrical or mechanical errors can be identified by inspection of the reconstructed near field. However, the integral-equation based methods [2]- [15] allow the field to be reconstructed on an arbitrary 3D surface enclosing the antenna which opens up a range of new applications. The new applications include but is not limited to artificial suppression of currents flowing on a part of the enclosing surface, e.g., a cable or a support structure, as well as pattern enhancement of noisy, truncated, or irregular measurements.

In this contribution we review the recently introduced higher-order INV-MoM [15] which is more computationally expensive than mode-based techniques, but allows for reconstruction of fields on arbitrary 3D surfaces. The smooth current expansion provided by the higher-order formulation along with a rigorous regularization scheme improve the stability and make the algorithm more robust against noise while providing computational savings. Nevertheless, the INV-MoM method is only competitive for small and medium-sized antennas. The INV-MoM and the mode-based SWE-PWE technique have been integrated into a single flexible software tool, DIATOOL, allowing field reconstruction using the most suitable algorithm for a specific application. Some of the processing capabilities of this tool are illustrated below with two examples based on measured field data obtained in the DTU-ESA spherical near-field test facility [16]. Both examples show a classical antenna diagnostics problem and the second one also illustrates the possibility of reconstructing details of the measured patterns which were not directly available due to noise.

II. Higher-Order Inverse Method of Moments

The higher-order INV-MoM [15] was introduced recently as an extension of previously available integral-equation based reconstruction techniques [2]- [14]. The method is aimed at computing tangential electric and magnetic fields on the reconstruction surface S enclosing an antenna, based on fields measured at discrete points outside the surface. On the reconstruction surface, the equivalent electric and magnetic surface current densities are defined as

$$\mathbf{J}_S = \hat{\mathbf{n}} \times \mathbf{H} \tag{1a}$$

$$\mathbf{M}_S = -\hat{\mathbf{n}} \times \mathbf{E}, \tag{1b}$$

where $\mathbf{E}$ and $\mathbf{H}$ are the fields just outside the surface of reconstruction. These equivalent currents are those corresponding to Love's equivalence principle since they produce zero field inside S. They also correspond to the tangential physical fields one would actually measure on S.

The measured field can now be written as

$$\mathbf{E}^{\text{meas}}(\mathbf{r}) = -\eta_0 \mathcal{L}\mathbf{J}_S + \mathcal{K}\mathbf{M}_S \tag{2}$$

where η_0 is the free-space impedance and the integral operators $\mathcal{L}$ and $\mathcal{K}$ are defined as

$$\mathcal{L}\mathbf{J}_S = j\omega\mu_0 \bigg[\int_S \mathbf{J}_S(\mathbf{r}')G(\mathbf{r},\mathbf{r}')\,dS' + \frac{1}{k_0^2}\int_S \nabla'_S \cdot \mathbf{J}_S(\mathbf{r}')\nabla G(\mathbf{r},\mathbf{r}')\,dS', \bigg] \tag{3a}$$

$$\mathcal{K}\mathbf{M}_S = \int_S \mathbf{M}_S(\mathbf{r}') \times \nabla G(\mathbf{r},\mathbf{r}')\,dS', \tag{3b}$$

where k_0 is the free-space wavenumber and $G(\mathbf{r},\mathbf{r}')$ is the scalar Green's function of free space. Equation (2) is referred to as the data equation, since it relates the measured data $\mathbf{E}^{meas}$ and the unknown surface current densities $\mathbf{J}_S$ and $\mathbf{M}_S$. This inverse source problem has been formulated previously by several authors, including [2], [4]- [12].

Love's equivalent currents in (1) constitute just one set of possible equivalent currents that radiate exactly the same field $\mathbf{E}^{\text{meas}}$ outside the reconstruction surface, but non-zero fields inside. The formulation is thus ambiguous and the desired physical current densities in (1) can only be obtained if additional a priori information is imposed [3], [14]. The desired currents in (1) are obtained by inforcing the a priori information that the fields radiated by ($\mathbf{J}_S$,$\mathbf{M}_S$) inside S must be zero. The formulation of the required boundary condition for the electric and magnetic fields leads to the equations

$$-\eta_0 \hat{\mathbf{n}} \times \mathcal{L}\mathbf{J}_S + \left(\hat{\mathbf{n}} \times \mathcal{K} + \frac{1}{2}\right)\mathbf{M}_S = 0, \qquad \text{(4a)}$$

$$-\left(\hat{\mathbf{n}} \times \mathcal{K} + \frac{1}{2}\right)\mathbf{J}_S - \frac{1}{\eta_0}\hat{\mathbf{n}} \times \mathcal{L}\mathbf{M}_S = 0 \qquad \text{(4b)}$$

for $\mathbf{r} \in S$. These expressions are referred to as the boundary condition equation.

A. Discretization

The surface of reconstruction is discretized using curvilinear patches of up to fourth order. The electric and magnetic surface currents on each patch are expanded as

$$\mathbf{X} = \sum_{m=0}^{M^u} \sum_{n=0}^{M^v-1} a^u_{mn}\mathbf{B}^u_{mn} + \sum_{m=0}^{M^v} \sum_{n=0}^{M^u-1} a^v_{mn}\mathbf{B}^v_{mn} \qquad (5)$$

where $\mathbf{X} = [\mathbf{J}, \mathbf{M}]$, a^u_{mn} and a^v_{mn} are unknown coefficients, M^u and M^v are the expansion orders along the u- and v-directions, and $\mathbf{B}^u_{mn}$ and $\mathbf{B}^v_{mn}$ are higher-order Legendre basis functions [17]. The current expansion above is then inserted in the data equation (2) and two orthogonal test vectors $(\hat{\theta}, \hat{\phi})$ are chosen at each measurement sampling point. This readily leads to the matrix equation

$$\bar{\mathbf{A}}\mathbf{x} = \mathbf{b}, \qquad (6)$$

where $\mathbf{x}$ is a vector of unknown basis function coefficients, $\mathbf{b}$ contains samples of the measured field, and $\bar{\mathbf{A}}$ is an $M \times N$ matrix with elements representing the field radiated by a particular basis function.

The current expansion is also inserted in the boundary condition equation (4) and here we choose a quasi-Galerkin scheme [15] which was found to perform better than pure Galerkin testing. This leads to the matrix equation

$$\bar{\mathbf{L}}\mathbf{x} = \mathbf{0}, \qquad (7)$$

where $\bar{\mathbf{L}}$ is a $P \times N$ matrix, whose elements represent the field radiated by a particular basis function, weighted by a particular testing function.

The discretization described above differs from other methods [2]- [14] in two important aspects. First, the geometry and unknown currents are represented by smooth polynomial functions. This results in improved efficiency, enhanced accuracy, and better resolution properties of the algorithm. Second, the testing of the boundary condition operator is performed *on* the actual surface of reconstruction. Other methods that include the boundary condition operator [3], [13], [14] employ an $\lambda/10$ inward offset version of the surface of reconstruction in combination with Dirac delta functions.

B. Regularization

The matrix equation (6) represents a discrete ill-posed problem and the singular values of $\mathbf{A}$ therefore decay to zero without any gap in the spectrum [18, p. 20]. To obtain a well-posed solution to the problem $\min \|\bar{\mathbf{A}}\mathbf{x} - \mathbf{b}\|_2$ regularization is needed by imposing a priori information about the solution. The a priori information used here is that of equation (7), i.e., the unknown currents on the reconstruction surface should satisfy the boundary condition. This a priori information not only ensures that the desired Love's equivalent currents are obtained, but also serves the purpose of making the solution well-posed. This differs from previously published works, as will be explained below.

A regularization method suitable for this purpose is that by Tikhonov, in which the regularized solution $\mathbf{x}_\lambda$ is determined by solving the least squares problem [19]:

$$\min\left\{\|\bar{\mathbf{A}}\mathbf{x}_\lambda - \mathbf{b}\|_2^2 + \lambda^2\|\bar{\mathbf{L}}\mathbf{x}_\lambda\|_2^2\right\}. \qquad (8)$$

The regularization parameter λ determines the weight given to minimizing the residual norm relative to the regularization term. It should be noted that this regularization scheme is fundamentally different from those of [3], [13]- [14], because the data equation and the boundary condition equation are used separately. If $\lambda = 0$ is used in the above expression, no regularization is applied, and $\mathbf{x}_0$ equals the standard least-squares problem, which is useless since it is dominated by rapid oscillations due to noise. When λ^2 is increased, more weight is put to the regularization term and $\mathbf{x}_\infty = 0$ in case $\mathbf{L}$ has full rank. A method for obtaining the optimum regularization parameter is the L-curve method [20].

III. Application Examples

The higher-order INV-MoM is now used to reconstruct the extreme near field for two practical cases: A corrugated horn antenna and three circular patch antenna elements in a large radiometer configuration.

A. Corrugated horn antenna

The corrugated horn antenna considered here is shown in Figure 1. The antenna is mounted on a metal frame which is covered by absorbers and the radiation pattern was measured in the DTU-ESA spherical near field test facility [16]. The radiation pattern at 10 GHz is shown in Figure 2 where an unexpected high on-axis cross-polar field component can be observed. The near field is then reconstructed on a circular cylinder as shown in Figure 3. The front face of the cylinder is located at the horn aperture at $z = 0$ and the radius of the cylinder corresponds to the actual horn radius (58.2 mm). The cross-polar field component radiated by the reconstructed currents is also evaluated in front of the aperture at $z = \lambda/4$ (see Figure 4) revealing a more clear picture of the reconstructed near field, see Figure 4. It is observed that the cross-polar field in front of the aperture looks distorted and lacks the expected symmetry.

The far field radiated by the reconstructed currents is also shown in Figure 2 along with the field obtained by truncating the measured SWE at the noise floor. At field levels below -40 dB, the field obtained by truncating the SWE looks like a low-pass filtered version of the noisy measured pattern. However, it is observed that the reconstructed far field do not agree with the truncated SWE field. The INV-MoM includes a priori information about the size and shape of the antenna, and one can therefore hope that the reconstructed pattern is more accurate than both the noisy measured pattern and the one obtained by truncating the SWE. It is obviously only possible to determine the most accurate pattern if the exact pattern is known and this was explored by using synthetic measured data. The radiation pattern of a corrugated horn, similar to the horn considered above, was evaluated by an accurate horn modeling tool and random noise was added in order to obtain a SWE with the same noise floor as the one obtained by the real measurements. The INV-MoM was then invoked with the noisy far field data as input. The surface of reconstruction was conformal to the geometrical model used in the horn modeling tool. Figure 5 shows the reference pattern obtained by the horn modeling tool, the noisy synthetic measurements, the reconstructed pattern obtained with INV-MoM, and the pattern obtained by truncating the SWE at the noise floor. The scale on the figure is relative to the co-pol peak at $\theta = 0$ and a random cut at $\phi = 46°$ has been selected. It is seen that the reconstructed pattern (dashed blue curve) captures very fine details of the reference pattern (black circles) whereas the truncated SWE pattern is simply a low-pass filtered version of the noisy measured pattern. This result leads to the conclusion that the INV-MoM can be used to improve the measurement accuracy and reconstruct details of the measured pattern which are not directly available due to the inherent measurement noise. This is accomplished by utilizing the information about the location, size, and shape of the antenna. Figure 6 shows the spectrum of the SWE coefficients for the reference field, the synthetic measured field, and the reconstructed field. It is observed that the INV-MoM is able to recover a part of the spectrum that was not readily available due to noise.

B. *Radiometer antenna elements*

The second test case considers three out of 69 circular patch antenna elements in the MIRAS instrument on ESA's SMOS satellite (see Figure 7). The radiation pattern of each antenna unit was measured at the DTU-ESA spherical near field test facility [16]. During this measurement campaign, two antenna units (BC03 and A01) were found to produce a higher cross-polar field than expected. Figure 8 shows the pattern of a correctly working unit (A01), a unit producing a 10 dB higher cross-polar component (BC03), and a unit producing a frequency-dependent cross-polar level (A05). These measured fields were used as input to the INV-MoM algorithm and the surface of reconstruction was chosen to be a small box enclosing the element. The reconstructed cross-polar field compo-

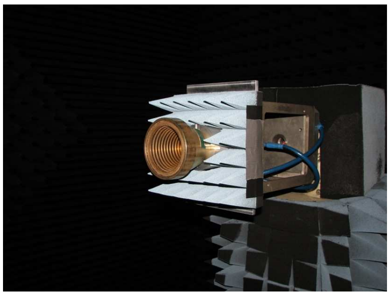

Fig. 1. Measurement setup for the corrugated horn.

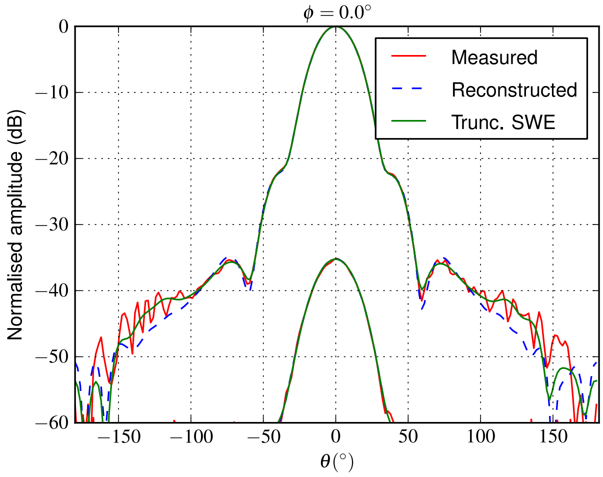

Fig. 2. Measured (solid red curve) and reconstructed (dashed blue curve) radiation patterns of the corrugated horn. The pattern obtained by truncating the SWE at the noise floor (n=13) is also shown (solid green curve). The curve with a peak of −35 dB represents the cross-polar component.

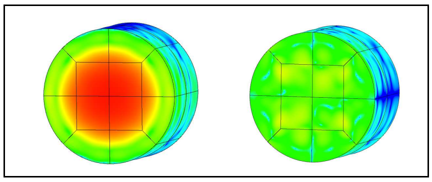

Fig. 3. Reconstructed x- and y-components of the electric field in dB-scale shown directly on the surface of reconstruction.

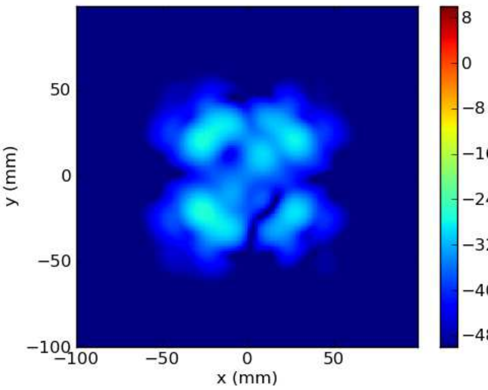

Fig. 4. Cross-polar component of the reconstructed field at the $z = \lambda/4$ plane. The scale is normalised such that 0 dB corresponds to the level of the co-polar peak in the $z = \lambda/4$ plane.

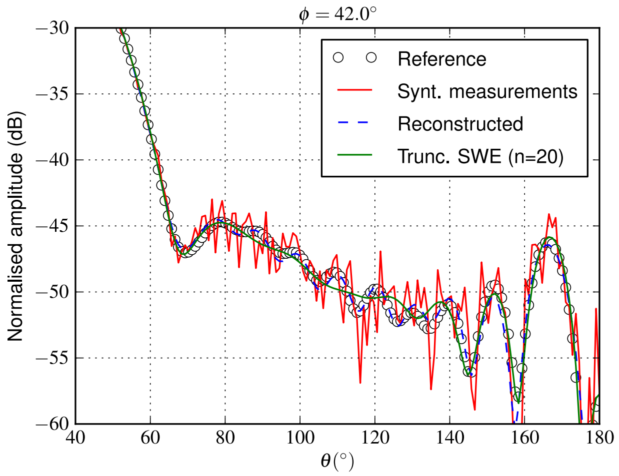

Fig. 5. Reference pattern (black dots), the synthetically measured data with added noise (solid red curve), the reconstructed pattern (dashed blue curve), and the truncated SWE pattern (solid green curve).

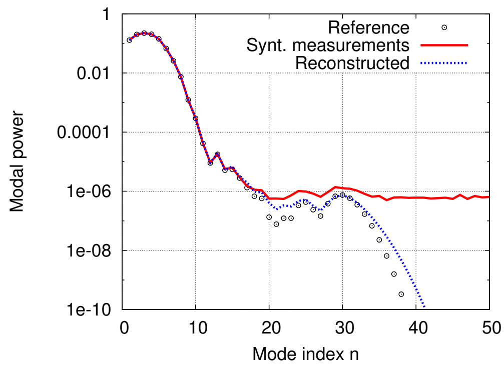

Fig. 6. Power content of the SWE coefficients for the reference pattern (black dots), the synthetically measured data with added noise (solid red curve), and the reconstructed pattern (dashed blue curve).

nents on the top surface of the thermal insulation foil ($z = -5$ mm) are shown in Figure 9. The correctly working unit A01 (left column) produced a frequency-independent symmetric cross-polar field component with a relatively low amplitude. Unit BC03 (centre column) produced a much higher cross-polar level and only two lobes instead of four. Unit A05 (right column) produced a cross-polar field that increases slightly with frequency and becomes more asymmetric at the highest frequency. This shows that even small errors in the cross-polar fields can be detected by the higher-order INV-MoM.

IV. Conclusions

This paper has described the higher-order Inverse Method of Moments technique for reconstruction of the extreme near field of an antenna. It's capabilities were illustrated with two antenna diagnostics applications where the reconstructed near field revealed anomalies of the antenna under test. Furthermore, an example was presented where the INV-MoM technique was used to enhance the measurement accuracy and reconstruct details of a measured pattern which were not

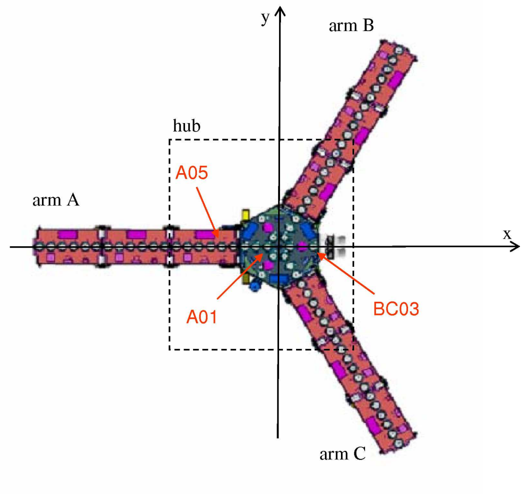

Fig. 7. Configuration of the MIRAS instrument on ESA's SMOS satellite. The three antenna elements investigated here are marked with red arrows.

directly available due to noise.

Acknowledgment

This work is supported by ESA/ESTEC within the ARTES 3/4 programme, ESTEC contract 22676/09/NL. The authors thank EADS CASA Espacio, Madrid, for permission to use the radiation pattern measurements of the MIRAS antenna units.

References

[1] C. Cappellin,O. Breinbjerg, A. Frandsen, "Properties of the transformation from the spherical wave expansion to the plane wave expansion," *Radio Science*, vol. 43, no. RS1012, doi:10.1029/2007RS003696, February 2008.

[2] T. K. Sarkar and A. Taaghol, "Near-field to near/far-field transformation for arbitrary near-field geometry utilizing and equivalent electric current and MoM," *IEEE Trans. Antennas Propagat.*, vol. 47, no. 3, pp. 566–573, Mar. 1999.

[3] K. Persson and M. Gustafsson, "Reconstruction of equivalent currents using a near-field data transformation - with radome applications," *Progress in Electromagnetics Research*, vol. 54, pp. 179–198, 2005.

[4] F. Las-Heras and T. K. Sarkar, "Evaluating near-field radiation patterns of commercial antennas," *IEEE Trans. Antennas Propagat.*, vol. 54, no. 8, pp. 2198–2207, Aug. 2006.

[5] Y. Alvarez, F. Las-Heras, and M. R. Pino, "Reconstruction of equivalent currents distribution over arbitrary three-dimensional surfaces based on integral equation algorithms," *IEEE Trans. Antennas Propagat.*, vol. 55, no. 12, pp. 3460–3468, Dec. 2007.

[6] Y. Alvarez, S. T, K, and F. Las-Heras, "Improvement of the sources reconstruction techniques: Analysis of the svd algorithm and the rwg basis functions," in *IEEE Antennas and Propagation Society International Symposium*, Honolulu, Hawaii, USA, July 2007.

[7] Y. Alvarez, F. Las-Heras, M. R. Pino, and J. A. Lopez, "Acceleration of the sources reconstruction method via the fast multipole technique," in *IEEE Antennas and Propagation Society International Symposium*, San Diego, CA, USA, July 2008.

[8] F. Mioc, J. A. Quijano, G. Vecchi, E. Martini, F. Milani, R. Guidi, L. J. Foged, and M. Sabbadini, "Source modelling and pattern enhancement for antenna farm analysis," in *30th ESA Antenna Workshop on Antennas for Earth Observation, Science, Telecommunication and Navigation Space Missions*, Noordwijk, The Netherlands, May 2008, pp. 555–559.

[9] T. F. Eibert and C. H. Schmidt, "Multilevel fast multipole accelerated inverse equivalent current method employing rao-wilton-glisson discretization of electric and magnetic surface currents," *IEEE Trans. on Antennas Propag.*, vol. 57, no. 4, pp. 1178–1185, 2009.

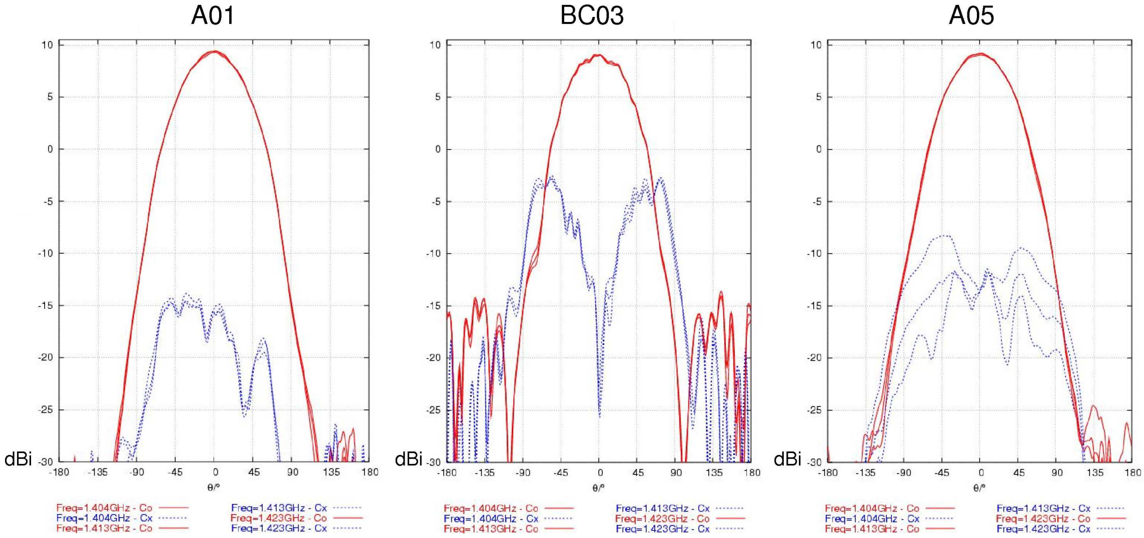

Fig. 8. Radiation patterns of the three selected MIRAS antenna units. Each plot contains three frequencies. Unit A01 (left) is working correctly, unit BC03 (centre) produces a high cross-polar field component, and unit A05 (right) produces a slightly increased cross-polar field level that deteriorates with increasing frequency.

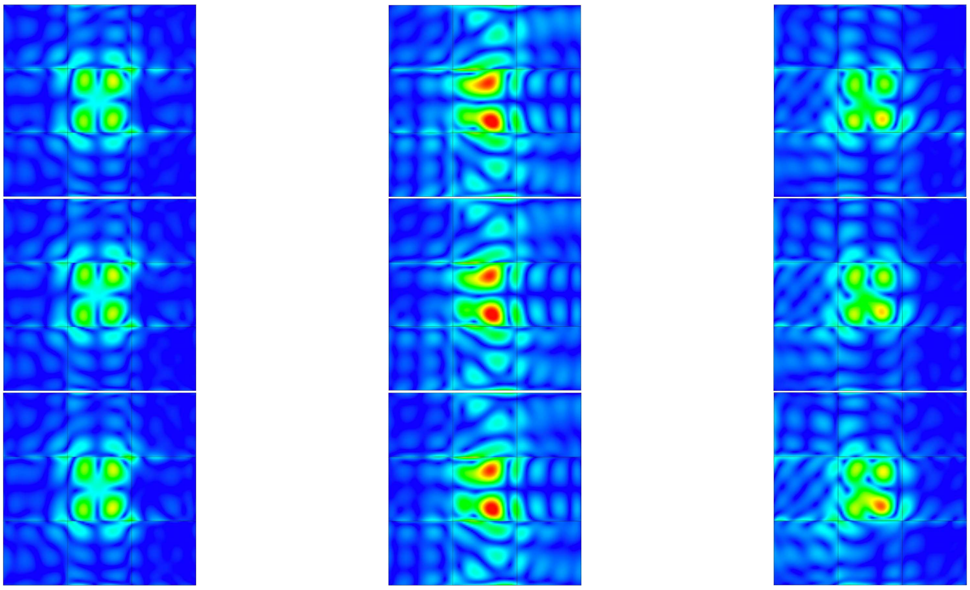

Fig. 9. Reconstructed cross-polar field (E_y) at $z = -5$ mm. From top to bottom the rows correspond to 1.404 GHz, 1.413 GHz, and 1.423 GHz. Left column: Correctly working unit A01. Centre column: Unit BC03 with high cross-polar field for all frequencies. Right column: Unit A05 with increasing cross-polar field levels for increasing frequency.

[10] Y. A. Lopez, F. L.-H. Andres, M. R. Pino, and T. K. Sarkar, "An improved super-resolution source reconstruction method," *IEEE Trans. Instrumentation and Measurement*, vol. 58, no. 11, pp. 3855–3866, Nov. 2009.

[11] C. H. Schmidt, Ismatullah, and T. F. Eibert, "Comparison of lower and higher order basis functions in inverse equivalent current methods," *Applied Computational Electromagnetics Society (ACES) Conference, Tampere, Finland*, April 2010.

[12] Y. Alvarez, F. Las-Heras, and M. R. Pino, "Antenna characterization using the sources reconstruction method," in *EuCAP Proceedings*, Barcelona, Spain, April 2010.

[13] J. L. A. Quijano and G. Vecchi, "Improved-accuracy source reconstruction on arbitrary 3-D surfaces," *IEEE Antennas and Wireless Propagation Letters*, vol. 8, pp. 1046–1049, 2009.

[14] ——, "Field and source equivalence in source reconstruction on 3D surfaces," *Progress in Electromagnetics Research*, vol. PIER-103, pp. 67–100, 2010.

[15] E. Jørgensen, P. Meaincke, C. Cappellin, and M. Sabbadini, "Improved source reconstruction technique for antenna diagnostics," in *Proceeedings of the 32nd ESA Antenna Workshop*, ESTEC, Noordwijk, The Netherlands, 2010.

[16] Homepage of the DTU-ESA Spherical Near Field Facility, *http://www.dtu.dk/centre/ems/English/research/facilities.aspx*, Technical University of Denmark, Lyngby, Denmark.

[17] E. Jørgensen, J. L. Volakis, P. Meincke, and O. Breinbjerg, "Higher order hierarchical Legendre basis functions for electromagnetic modeling," *IEEE Transactions on Antennas and Propagation*, vol. 52, no. 11, pp. 2985–2995, Nov. 2004.

[18] P. C. Hansen, *Rank-Deficient and Discrete Ill-Posed Problems*. Philadelphia, PA: Society for Industrial and Applied Mathematics, 1998.

[19] ——, "The truncated SVD as a method for regularization," *BIT*, vol. 27, pp. 534–553, 1987.

[20] ——, "Analysis of discrete ill-posed problems by means of the L-curve," *SIAM Review*, vol. 34, pp. 561–580, Dec. 1992.